Out-of-Equilibrium Dynamics of a Grid-Like Fe(II) Spin Crossover Dimer Triggered by a Two-Photon Excitation

Jose de Jesus Velazquez-Garcia[a]*, Krishnayan Basuroy[a], Joanne Wong[b], Serhiy Demeshko[b], Franc Meyer[b], Insik Kim[c], Robert Henning[c], Yannic U. Staechelin[d], Holger Lange[e,f] and Simone Techert[ag]

[a]Photon Science - Structural Dynamics in Chemical Systems, Deutsches Elektronen-Synchrotron DESY, Notkestraße 85, Hamburg, 22607, Germany

[b]Institut für Anorganische Chemie, Georg-August-Universität Göttingen, Tammannstraße 4, Göttingen, 37077, Germany

[c]Center for Advanced Radiation Sources, The University of Chicago, Argonne National Laboratory, 9700 South Cass Ave, Lemont, Illinois, 90439, USA

[d]Institute of Physical Chemistry, Universität Hamburg, Martin-Luther-King-Platz 6, Hamburg, 20146, Germany

[e]The Hamburg Center for Ultrafast Imaging, Universität Hamburg, 22761 Hamburg, Germany

[f]Institute of Physics and Astronomy, Universität Potsdam, Karl-Liebknecht-Str. 24, 14476 Potsdam, Germany

[g]Institut für Röntgenphysik, Georg-August-Universität Göttingen, Friedrich-Hund-Platz 1, Göttingen, 37077, Germany

Supplementary information

S.I.1 Variable Temperature Single Crystal XRD

    FE2 structure at 100K

    Structural reorganisaiton

    Structural analysis

S.I.2 Optical Transient Absorption Spectroscopy

    Solvent response

    Recovery dynamics

S.I.3 Time Resolved Photocrystallography

    Ortep plots

    Photodifference maps

    Correlation plot

    Structural reorganisation

Estimate of temperature difference

References

S.I.1 Variable Temperature Single Crystal XRD

FE2 structure at 100K

Table S1. Crystal data and Structure refinement parameters of **FE2** at 100 K.

Temperature	100 K
Empirical Formula	$2(C_{46}H_{32}FeN_{12})$, $4(BF_4)$, $2(C_2H_3N)$
Crystal colour/habit	Black/block
Crystal size (mm)	(0.200x0.120x0.100)
Crystallizing solvent	Acetonitrile
Crystal system/ Space group	Monoclinic/ $P2_1/c$
a (Å)	23.520 (5)
b (Å)	15.310 (3)
c (Å)	26.870 (5)
α (°)	90
β (°)	110.74 (3)
γ (°)	90
Volume (Å^3)	9049 (4)
Z/Z'	4/1
Molecular Weight	2046.72
Calculated density (g/cm3)	1.502
F(000)	4176
Radiation	Synchrotron (λ=0. 61990 Å)
θ range (°)	0.864/22.656
Scan type	ϕ
Measured reflections	117667
Unique reflections	17941
Observed reflections [$\|F\|> 4\sigma(F)$]	16717
Final R (%)	6.02
wR2 (%)	17.13
Good-of-fit on F^2(S)	1.048
$\Delta\rho$ max (e. Å^{-3})	2.466
$\Delta\rho$ min (e. Å^{-3})	-0.835
No of restrains/parameters	218/1455
Data [$\|F\|> 4\sigma(F)$]-to-parameter ratio	11.49:1

Table S2. Selected bond lengths and bond angles for compound **FE2** at 100K

| Bond lengths (Å)		Bond angles (°)			
Fe(A)-N1	1.9570 (20)	N2-Fe(A)-N9	100.95 (8)	N15-Fe(B)-N13	160.34 (8)
Fe(A)-N2	1.8991 (18)	N2-Fe(A)-N3	79.89 (8)	N15-Fe(B)-N19	90.01 (8)
Fe(A)_N3	1.9640 (20)	N2-Fe(A)-N1	80.98 (8)	N21-Fe(B)-N15	93.91 (8)
Fe(A)-N7	1.9760 (20)	N2-Fe(A)-N7	98.01 (8)	N21-Fe(B)-N13	89.61 (8)
Fe(A)-N8	1.8957 (18)	N9-Fe(A)-N7	160.96 (7)	N21-Fe(B)-N19	160.39 (8)
Fe(A)-N9	1.9730 (18)	N3-Fe(A)-N9	94.47 (8)	N20-Fe(B)-N15	102.60 (8)
Fe(B)-N13	1.9720 (20)	N3-Fe(A)-N7	90.47 (8)	N20-Fe(B)-N21	79.75 (8)
Fe(B)-N14	1.9010 (20)	N8-Fe(A)-N2	177.86 (8)	N20-Fe(B)-N13	97.06 (8)
Fe(B)-N15	1.9707 (19)	N8-Fe(A)-N9	80.24 (8)	N20-Fe(B)-N19	80.65 (8)
Fe(B)-N19	1.9730 (20)	N8-Fe(A)-N3	101.83 (8)	N14-Fe(B)-N15	79.57 (9)
Fe(B)-N20	1.9013 (19)	N8-Fe(A)-N1	97.30 (8)	N14-Fe(B)-N21	102.65 (8)
Fe(B)-N21	1.9676 (19)	N8-Fe(A)-N7	80.75 (8)	N14-Fe(B)-N20	176.71 (8)
		N1-Fe(A)-N9	88.83 (8)	N14-Fe(B)-N13	80.79 (9)
		N1-Fe(A)-N3	160.87 (7)	N14-Fe(B)-N19	96.95 (8)
		N1-Fe(A)-N7	92.51 (8)	N13-Fe(B)-N19	93.13 (8)
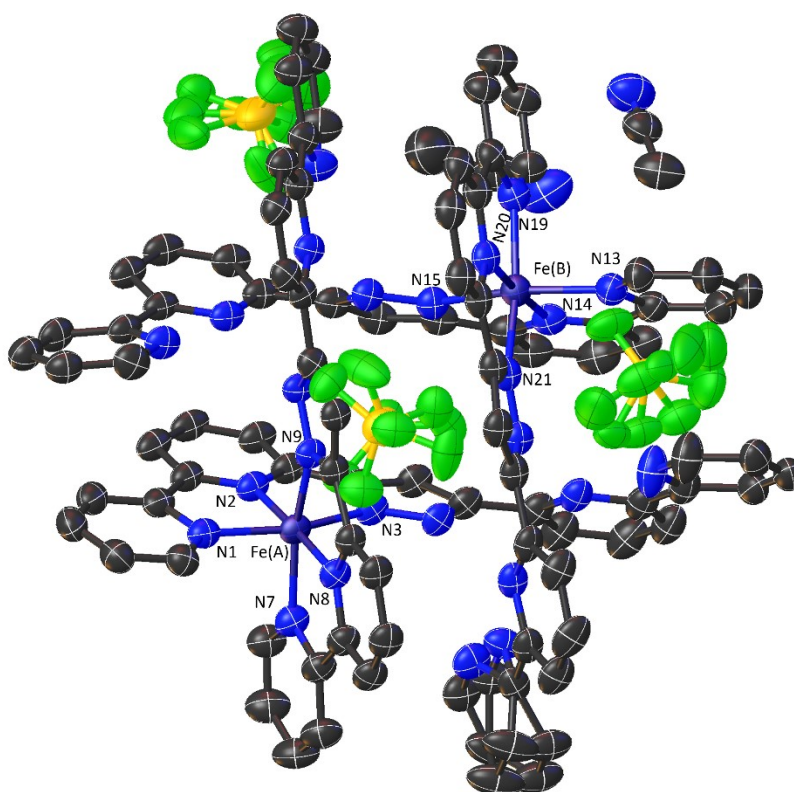
Figure S1. Asymmetric unit of the FE2 grid at 100K. Hydrogen atoms are omitted for clarity.
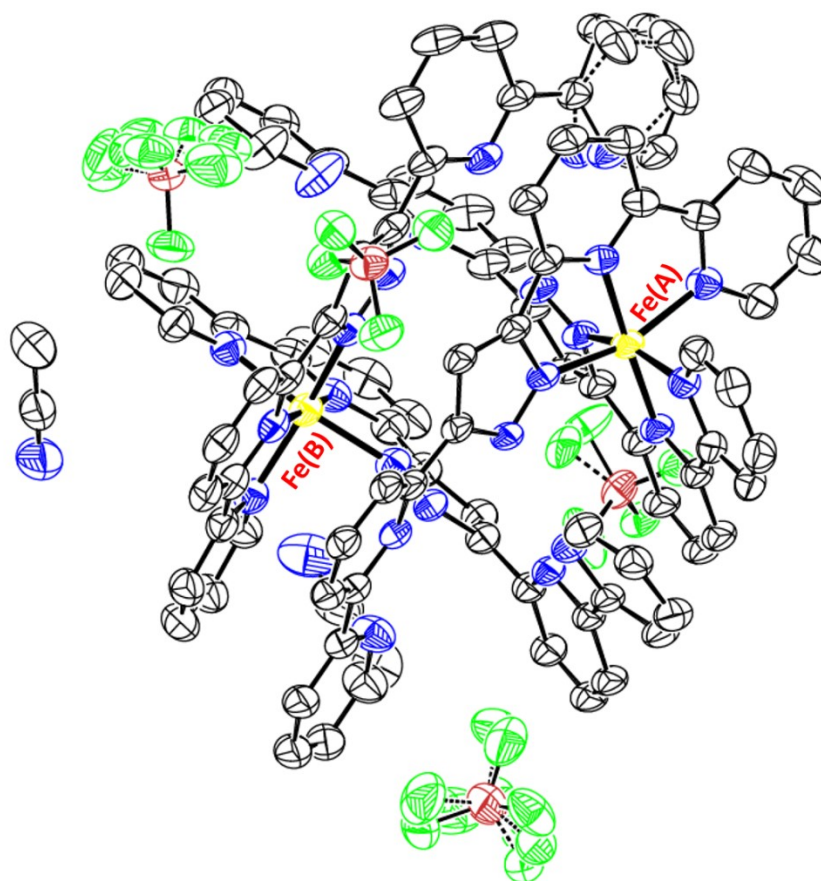
Figure S2. Thermal ellipsoid plot (50% of probability) for FE2 at 100K. Hydrogen atoms are omitted for clarity.
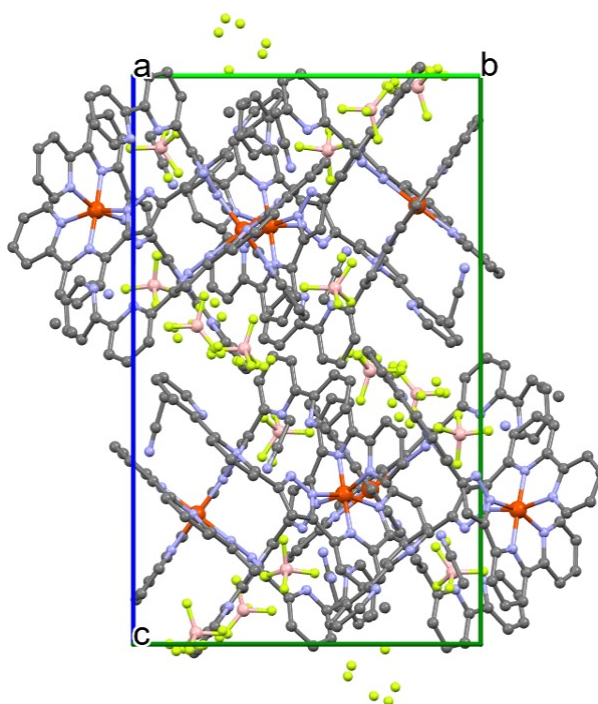

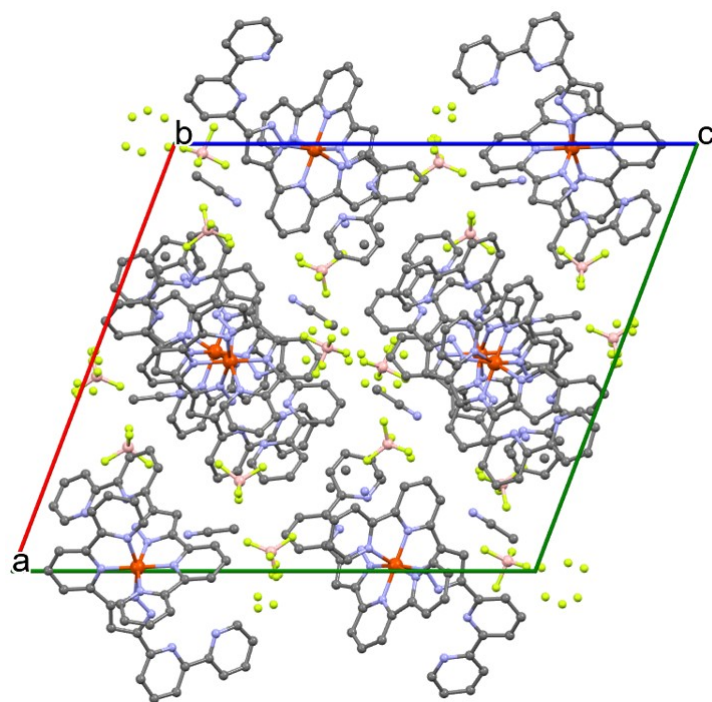Figure S3. Packing of molecules down crystallographic '*a*' axis. Hydrogen atoms are omitted for clarity.

Figure S4. Packing of molecules down crystallographic '*b*' axis. Hydrogen atoms are omitted for clarity.
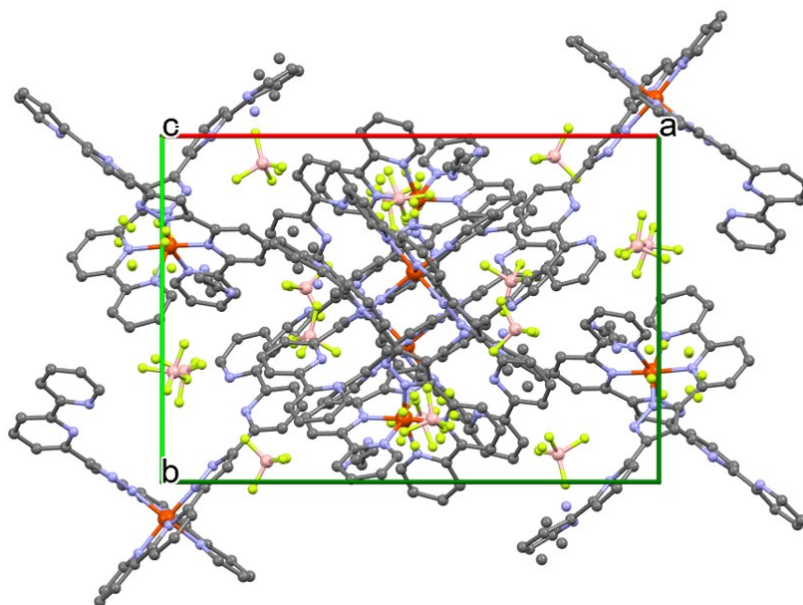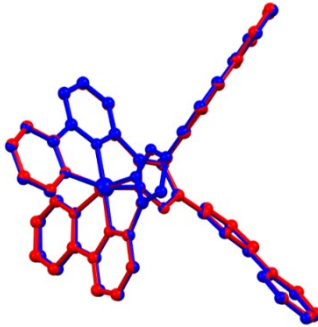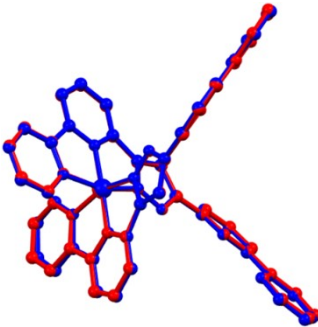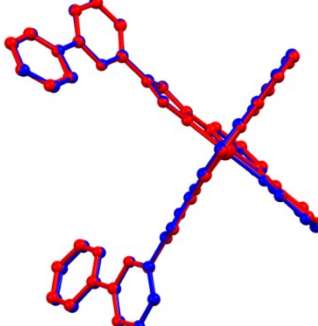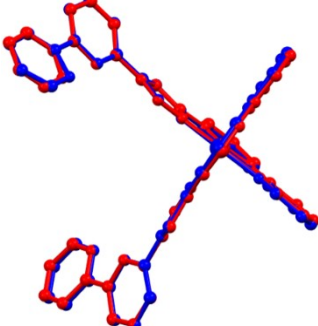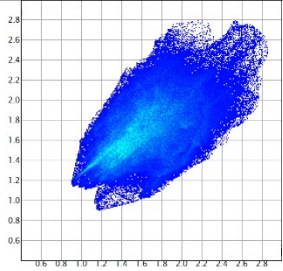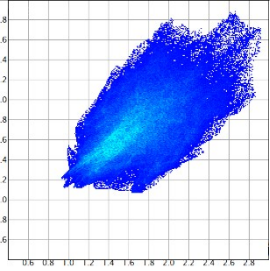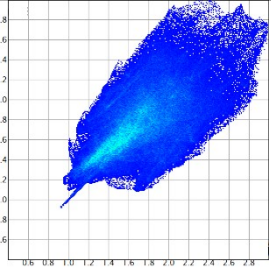

Figure S5. Packing of molecules down crystallographic '*c*' axis. Hydrogen atoms are omitted for clarity.

Structural reorganisation

Table S3. Structural data that provides a basic description of **FE2** upon heating.

Structural parameter	100 K	290 K	390 K
Fe(A)-N6 polyhedron			
<Fe1-N> (Å)	1.944 (2)	1.950 (1)	1.953 (2)
S(Oh)	1.923	1.966	2.033
S(itp)	12.091	12.027	11.934
Σ (°)	84.8641	83.9470	85.2119
Θ (°)	276.6292	279.7725	285.9149
ζ (Å)	0.1876	0.1979	0.1869
Vp (Å³)	9.514	9.591	9.631
Fe(B)-N6 polyhedron			
<Fe2-N> (Å)	1.948 (2)	1.951 (2)	1.956 (3)
S(Oh)	2.054	2.089	2.118
S(itp)	11.485	11.544	11.477
Σ (°)	85.9324	86.1841	86.8147
Θ (°)	292.9054	296.4063	300.55
ζ (Å)	0.1863	0.1791	0.1591
Vp (Å³)	9.541	9.585	9.647
Molecular Scale (Superposition of structures)			
	100K (blue) & 290 K (red)		100K (blue) & 390 K (red)
Fe(A)			
Maximum RMSD	0.2071		0.2698
Average RMSD	0.0685		0.0900
Fe(B)			
Maximum RMSD	0.1788		0.3057
Average RMSD	0.0739		0.1018
Unit cell Changes			
a (Å)	23.520 (5)	23.650 (5)	23.840 (5)
b (Å)	15.310 (3)	15.630 (3)	15.790 (3)
c (Å)	26.870 (5)	27.020 (5)	27.050 (5)
β (°)	110.74 (3)	110.75 (3)	110.78 (3)
V (Å³)	9049 (4)	9344 (4)	9520 (4)
Crystal packing			

Intermolecular interactions			
Separation between π-π planes (Å)	4.039	4.161	4.218
Crystal density	1.502	1.455	1.426

$\Sigma=\Sigma^{12}_{i=1}$ |90 - ϕ_i|, the sum of the angular deviations from 90° for the 12 cis angles (ϕ_i)[1,2], $\Theta = \Sigma^{24}_{i=1}$|60 -$\theta_i$|[3], $\zeta=(Fe-N_i)$ - <Fe-N>[4]. Information about S(Oh) and S(itp) is provided in the structural analysis section.

Structural Analysis

The Octadist program[5] was used to determine the <Fe-N> bond length and the angular distortion parameter that describe the octahedral coordination environment of the metal centres in the **FE4** grid. The angular distortion parameter, Θ, is the sum of the deviations from 60° of the twenty-four N-Fe-N angles, six per pseudo three-fold axis, measured on a projection of opposite triangular faces of the $\{FeN_6\}$ octahedron, orientated by superimposing the face centroids (Figure S6).[3,6]

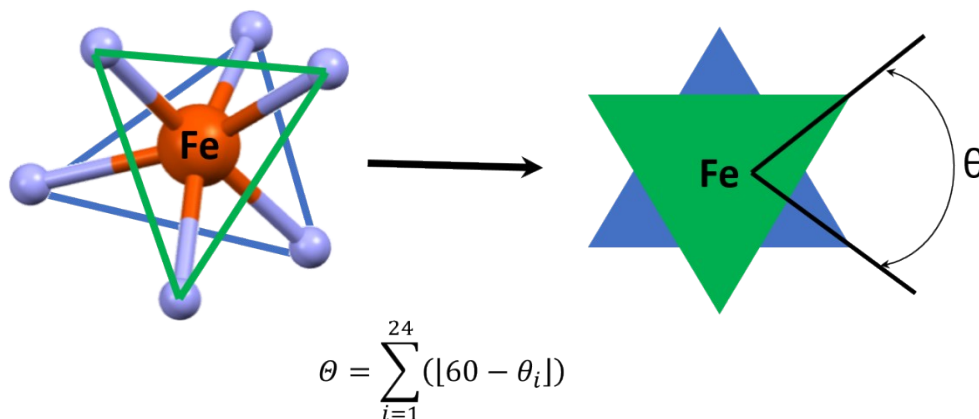$$\Theta = \sum_{i=1}^{24}(\lfloor 60 - \theta_i \rfloor)$$

Figure S6. Environment of Fe^{II} ions and definition of the θ angle and the angular distortion parameter (Θ).[3,6]

For comparison, continuous shape measurements (CShM) were also used to characterise the relative deviation of the metal coordination spheres in **FE4** from ideal polyhedra described by a particular point symmetry group (Table S2).[7] Mathematically, CShM of the coordination polyhedron Q with the geometric centre $\vec{q}_0$ relative to an ideal polyhedron P is expressed as:

$$S_Q = min\left[\frac{\sum_{i=1}^{N}|\vec{q}_i - \vec{p}_i|^2}{\sum_{i=1}^{N}|\vec{q}_i - \vec{q}_0|^2}\right] \times 100 \qquad (1)$$

where $\vec{q}_i$ and $\vec{p}_i$ are the position vectors for atoms of two polyhedral. CShM relative to an ideal octahedron (S(Oh)) and an ideal trigonal prism (S(itp)) were calculated using the SHAPE program[8]. The calculation of S(Oh) and S(itp) were performed for all crystallographic-symmetry independent metal atoms.

It is well-known that the $\{FeN_6\}$ coordination sphere of LS Fe^{II} ions is more regular, i.e., closer to an ideal octahedron. Therefore, the S(Oh) parameter is small and closer to 0, while the parameter S(itp) >> 0. Contrary, Fe^{II} ions in the HS state are characterised by a more irregular structure with structural parameters S(Oh) >> 0 and S(itp) closer to zero.

S.I.2 Optical Transient Absorption Spectroscopy
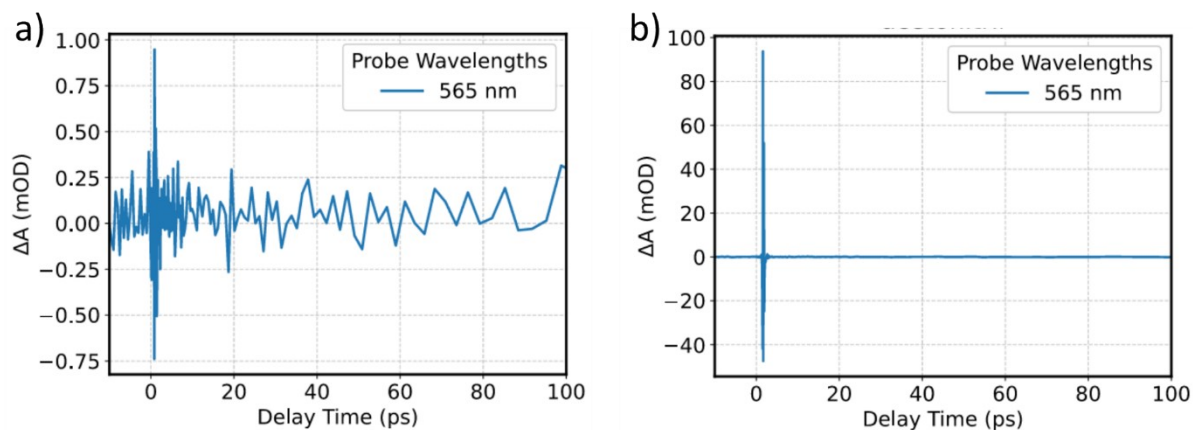
Solvent response

Figure S7. Measurements of the solvent at a) 400nm and b) 800nm excitation.
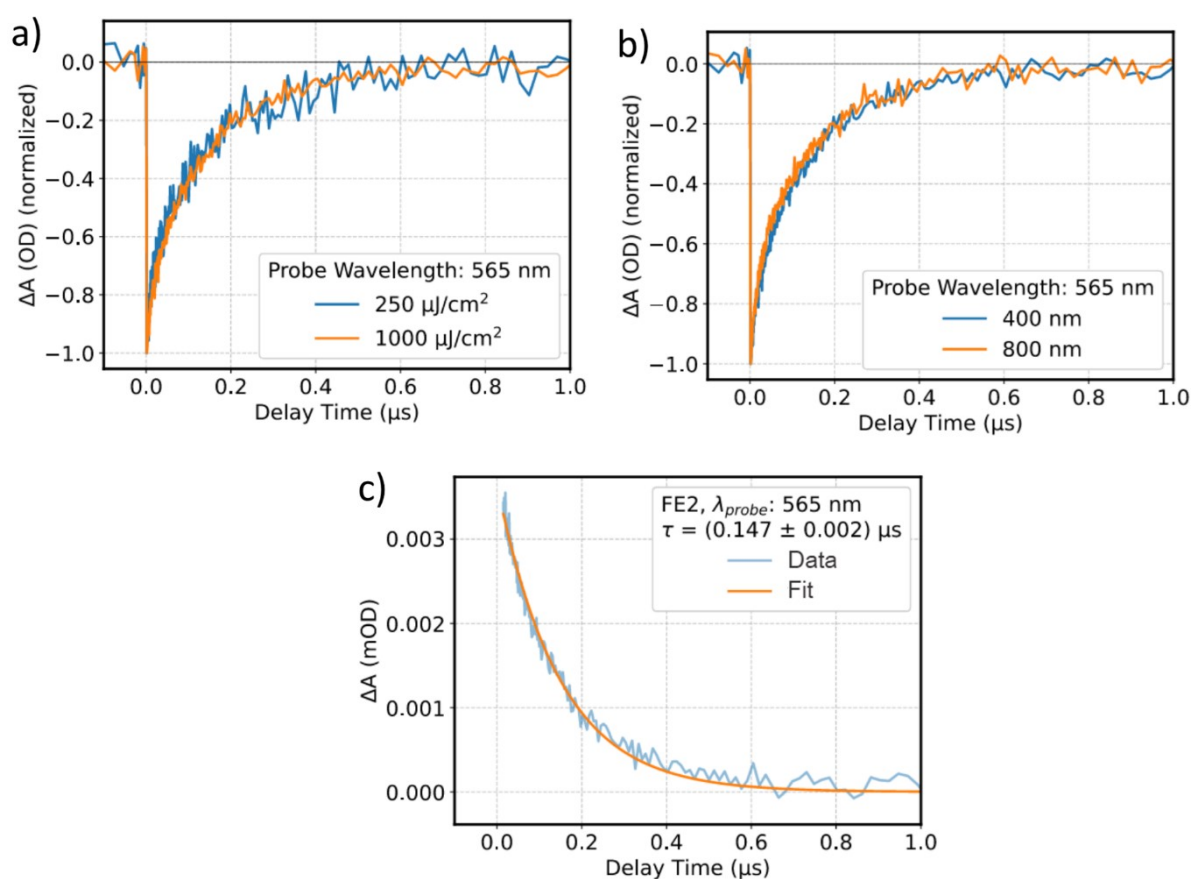
Recovery dynamics

Figure S8. Recovery dynamics a) 400nm excitation at two different fluences, b) 400nm vs 800nm excitation and c) experimental data with exponential fitting for probe at 565nm.

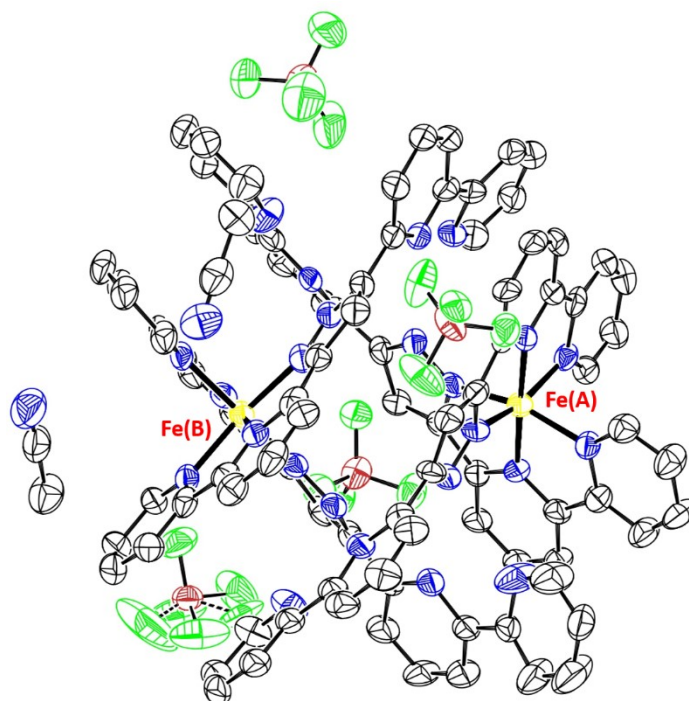## S.I.3 Time Resolved Photocrystallography

Ortep plots

Figure S9. Thermal ellipsoid plot (50% of probability) for FE2, laser OFF data set. Hydrogen atoms are omitted for clarity.
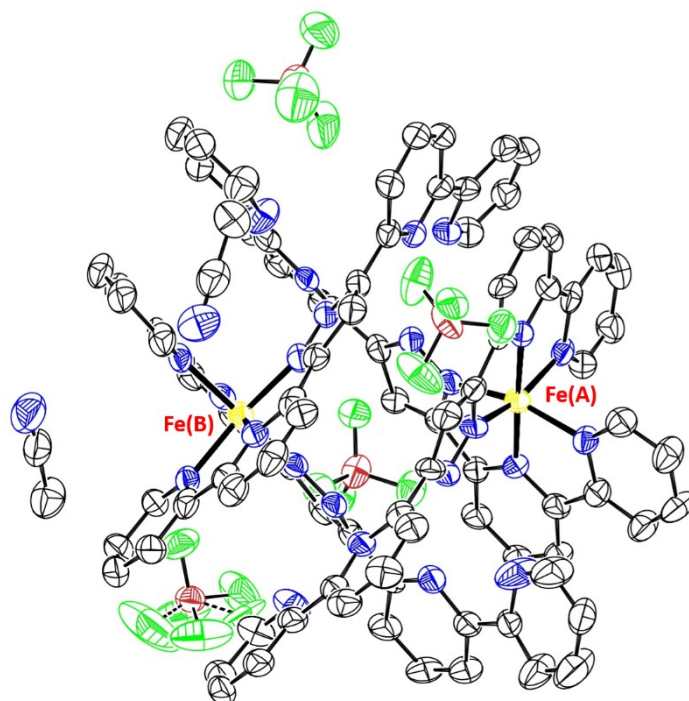

Figure S10. Thermal ellipsoid plot (50% of probability) for FE2, laser ON data set. Hydrogen atoms are omitted for clarity.

Photodifference maps

The photodifference map offers an initial insight into structural changes occurring upon excitation. These maps are obtained by subtracting the Fourier-map generated from the laser-OFF data ($\rho^{laserOFF}$(**r**)) from the Fourier map generated from the laser-ON data ($\rho^{laserON}$(**r**)):

$$\Delta\rho(r) = \rho^{laserON}(r) - \rho^{laserOFF}(r) \qquad (2)$$

The phases (φ) of the experimental laser-ON and laser-OFF structure factors (**F**) are assumed equal to the calculated phases of the reference dataset collected with monochromatic radiation (ϕ^{Ref}). For the **FE2** that is the dataset collected at PETRA III at 100K during the VT-SCXRD. Then equation 2 can be express for each reflection (**H**) as:

$$\Delta\rho(r) = \frac{1}{V}\sum_{H}\left[|F^{laserON}(H)| - |F^{laserOFF}(H)|\right]e^{i\varphi^{Ref}}e^{-i2\pi H\cdot r}$$

$$(3)$$

In the case of the LaueUtil toolkit[9,10], the software works with the Ratio method[11]. Here, the software works with the ratios (R) of laser-ON and laser-OFF intensities for each reflection **H**:

$$R(H) = \frac{I^{ON}(H)}{I^{OFF}(H)} \qquad (4)$$

Then the experimental absolute structure factors for the laser-ON and laser-OFF data can be expressed as:

$$|F^{laserON}(H)| = \left[R(H)K^{Ref}I^{Ref}(H)\right]^{1/2} \qquad (5)$$

$$|F^{laserON}(H)| = \left[K^{Ref}I^{Ref}(H)\right]^{1/2} \qquad (6)$$

with K^{ref} as the scale factor obtained from the refinement of the reference structure and I^{ref}(**H**) as the experimental intensity of reflection **H** obtained from the reference dataset.

Therefore, the photodifference map can be express based on experimental ratios as:

$$\Delta\rho(r) = \frac{1}{V}\sum_{H}\{[R(H)]^{1/2} - 1\}\left[K^{Ref}I^{Ref}(H)\right]^{1/2}e^{i\varphi^{Ref}}e^{-i2\pi H\cdot r}$$

$$(7)$$

More information about photodifference maps can be found in the literature[12]

Correlation plot

Correlation plots are typically used prior structure refinements to compare different data sets. These plots compare the individual ratios (R(**H**)) between two datasets, ensuring that the ratios are present in both datasets. Although these plots do not provide information about the absolute structure light-induced system response for each data set, they can estimate the relative light-induced system response in different data sets.[13,14] The correlation between the 200ps and 500ps data sets of **FE2** is reasonable, as shown in Figure S11. The yellow line represents the ideal case of a perfect correlation between both data sets (45°), whereas the green line indicates the average tendency of the comparison between the 200*ps* and 500*ps* datasets.
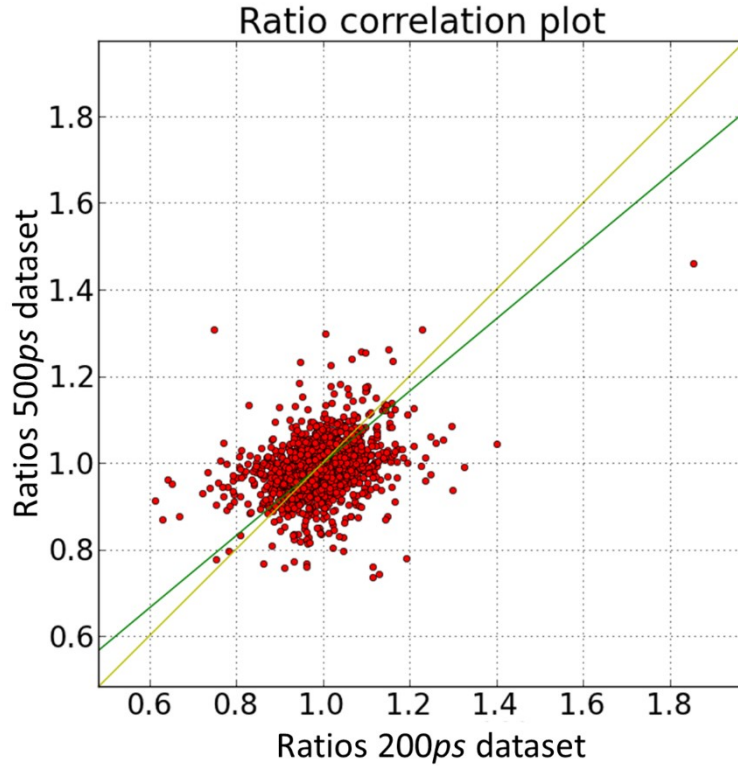
Figure S11. Correlation plot of time-resolved ratios between the 200*ps* and 500*ps* data sets.

Structural reorganisation

Table S4. Calculated Δ<Fe-N>, ΔΘ (°) and % ΔX_{HS} for the **FE2** grid upon excitation using laser OFF and laser ON datasets at different I/σ(I) and resolution cutoffs.

Resolution (Å)	Fe(A)			Fe(B)		
	Δ<Fe-N> (Å)	ΔΘ (°)	% ΔX_{HS}	Δ<Fe-N> (Å)	ΔΘ (°)	% ΔX_{HS}
Sigma cutoff I/σ(I) ≥ 2						
0.85	0.0018	1.6701	0.9	0.0006	1.052	0.3
0.90	0.0019	1.2282	0.95	0.0015	0.8537	0.75
0.95	0.0022	1.4377	1.1	0.0001	1.5573	0.05
1.00	0.0035	1.0093	1.75	0.0003	0.2625	0.15
Sigma cutoff I/σ(I) ≥ 3						
0.85	0.0022	-0.0851	1.1	0.0014	-0.0378	0.7
0.90	0.0016	0.831	0.8	0.0022	0.5877	1.1
0.95	0.0022	0.1751	1.1	0.0016	0.3331	0.8
1.00	0.0023	-0.8686	1.15	0.0025	0.3796	1.25

Estimate of temperature difference

A way to estimate the temperature difference between two different data sets collected at different temperatures is obtained from temperature-Wilson plots. The plots are obtained by a scale-factor refinement of the low temperature data (e.g. 100K) with the high-temperature data (e.g.290K) structural model and plotting the $\ln(I_{100K}/I_{290K})$. The slope of the dependence of $\ln(I_{100K}/I_{290K})$ with $(\sin\theta/\lambda)^2$ gives

the overall increase of isotropic atomic motion, ΔB (equation 8), which is associated with temperature difference between the data sets.[15]

$$ln\left(\frac{I_{100K}}{I_{290K}}\right) = -2\Delta B_{100K-290K}(sin\theta/\lambda)^2$$

(8)

An analogous equation is used to calculate the temperature increase during the photo-crystallographic experiments. The energy deposited by the laser pulse largely exceed the energy necessary for the LS to HS transition, which results in some heat diffusion and global warming. A modified Wilson plot, known as photo-Wilson plot, is then used to estimate the lase-induced temperature increase due to heat dissipation in a similar way as described above for the temperature-Wilson plots. From the photo-Wilson plot is possible to calculate the variation of the isotropic temperature factor (ΔB)[15]:

$$ln\left(\frac{I_{ON}}{I_{OFF}}\right) = -2\Delta B(sin\theta/\lambda)^2$$

(9)

where, I_{ON} and I_{OFF} are the laser-ON and laser-OFF intensities. Note that, in both cases, intensities must be brought to the same scale before calculating the value of ΔB.
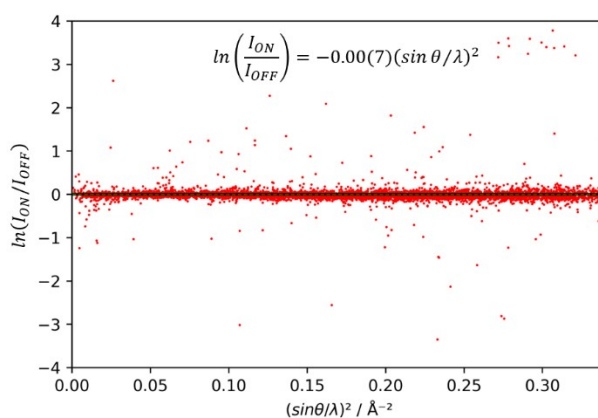

Figure S12. Photo-Wilson plot of **FE2**

References

1 P. Guionneau, M. Marchivie, G. Bravic, J.-F. Létard and D. Chasseau, in *Spin Crossover in Transition Metal Compounds II*, eds. P. Gütlich and H. A. Goodwin, Springer Berlin Heidelberg, Berlin, Heidelberg, 2004, pp. 97–128.

2 M. A. Halcrow, *Chem. Soc. Rev.*, 2011, **40**, 4119–4142.

3 M. Marchivie, P. Guionneau, J.-F. Létard and D. Chasseau, *Acta Crystallogr. B*, 2005, **61**, 25–28.

4 M. Buron-Le Cointe, J. Hébert, C. Baldé, N. Moisan, L. Toupet, P. Guionneau, J. F. Létard, E. Freysz, H. Cailleau and E. Collet, *Phys Rev B*, 2012, **85**, 064114.

5 R. Ketkaew, Y. Tantirungrotechai, P. Harding, G. Chastanet, P. Guionneau, M. Marchivie and D. J. Harding, *Dalton Trans*, 2021, **50**, 1086–1096.

6 M. Marchivie, P. Guionneau, J.-F. Létard and D. Chasseau, *Acta Crystallogr. B*, 2003, **59**, 479–486.

7 H. Zabrodsky, S. Peleg and D. Avnir, *J. Am. Chem. Soc.*, 1992, **114**, 7843–7851.

8 M. Llunell, D. Casanova, J. Cirera, P. Alemany and S. Alvarez, *SHAPE program, version 2.1*, Barcelona, 2003.

9 J. A. Kalinowski, A. Makal and P. Coppens, *J. Appl. Crystallogr.*, 2011, **44**, 1182–1189.

10 J. A. Kalinowski, B. Fournier, A. Makal and P. Coppens, *J. Synchrotron Radiat.*, 2012, **19**, 637–646.

11 P. Coppens, M. Pitak, M. Gembicky, M. Messerschmidt, S. Scheins, J. Benedict, S. Adachi, T. Sato, S. Nozawa, K. Ichiyanagi, M. Chollet and S. Koshihara, *J. Synchrotron Radiat.*, 2009, **16**, 226–230.

12 B. Fournier and P. Coppens, *Acta Crystallogr. A*, 2014, **70**, 291–299.

13 P. Coppens, A. Makal, B. Fournier, K. N. Jarzembska, R. Kamiński, K. Basuroy and E. Trzop, *Acta Crystallogr. B*, 2017, **73**, 23–26.

14 B. Fournier and P. Coppens, *Acta Crystallogr. A*, 2014, **70**, 514–517.

15 M. S. Schmøkel, R. Kamiński, J. B. Benedict and P. Coppens, *Acta Crystallogr. A*, 2010, **66**, 632–636.